OPTICS

Insight into human photoreceptor function: Modeling optoretinographic responses to diverse stimuli

Denise Valente[1,2]*, Kari V. Vienola[1,3], Robert J. Zawadzki[1,4], Ravi S. Jonnal[1]

Optoretinography is an emerging method for detecting and measuring functional responses from neurons in the living human retina. Its potential applications are compelling and broad, spanning clinical assessment of retinal disease, investigation of fundamental scientific questions, and rapid evaluation of experimental therapeutics for blinding retinal diseases. Progress in all these domains hinges on the development of robust methods for quantifying observed responses in relation to visible stimuli. In this work, we describe an optoretinographic imaging platform: full-field swept-source optical coherence tomography with adaptive optics, measure cone responses in two healthy volunteers to a variety of stimulus patterns, and propose a simple model for predicting and quantifying responses to those stimuli.

INTRODUCTION

Photoreceptors are specialized neurons responsible for phototransduction, a biochemical process that initiates vision. Therefore, the assessment of these cells' function is a critical step when assessing visual health. Blinding diseases whose pathogenesis primarily involves photoreceptors include age-related macular degeneration (AMD), retinitis pigmentosa (RP), and other inherited retinal degenerations (IRDs) such as achromatopsia, pattern dystrophy, and Stargardt's disease. AMD is the most prevalent of these, affecting nearly 200 million people worldwide, with projections estimating that this number will reach 300 million within the next two decades (*1*), making it the leading cause of irreversible blindness globally. Worldwide prevalence of RP and Stargardt's disease is ~1 million each (*2*, *3*), with IRDs affecting ~5.5 million individuals in total (*4*).

At present, the established means of assessing photoreceptor function are subjective tests such as visual fields (*5*), visual acuity (VA) (*6*), and contrast sensitivity (*7*). Less frequently used are objective measures like the electroretinogram (ERG) (*8*) and multifocal ERG (mfERG) (*9*). Despite their clinical utility, all of these methods have inherent limitations. VA tests only assess central function, and all subjective tests are affected by sources of noise such as fatigue, attention, and learning effects. While ERG testing is objective, it is slightly invasive and lacks spatial resolution. Conversely, mfERG offers spatial localization of up to 1° but can be a demanding test, requiring stable fixation for 10 min or more, and is thus rarely ordered by clinicians. While perimetry and mfERG provide some spatial localization, neither provides accompanying information about the retinal structure in those locations.

Photoreceptor health can also be assessed using structural imaging. Optical coherence tomography (OCT) offers high-resolution three-dimensional (3D) imaging of the laminar structure of the retina. It has become a standard of ophthalmic care by providing structural biomarkers of retinal disease (*10*). However, OCT-based anatomical biomarkers remain an imperfect predictor of functional state (*11*). Moreover, in the context of therapies designed to protect or restore visual function, structural changes defining an endpoint may represent unrecoverable vision loss.

In recent years, combination of phase-sensitive OCT (*12*, *13*) with visible stimuli has led to the discovery of nanometer-scale light-evoked changes in the photoreceptor outer segments (OSs) consisting of reproducible patterns of contraction and elongation that mostly scale with the stimulus dose (*14*–*21*). This signal has emerged as a favored tool in the broader set of methods used to measure retinal neural function optically, which has been called optoretinography (ORG). While much of the initial work has been demonstrated with time-consuming methods and small fields of view, strategies have been developed to measure ORG responses across the macula with both speed and spatial resolution rivaling or exceeding that of VA, microperimetry, and ERG/mfERG while providing structural information in tandem (*21*–*23*). Moreover, ORG investigators have recently shown that the technique is sensitive to disease-related changes at the level of single photoreceptors (*24*, *25*). Of course, at present we know neither the ORG's comparative sensitivity to disease-related dysfunction nor its specificity for pathogenic mechanisms. Thus, it should be regarded as a complement to existing clinical tools.

Besides phototransduction, which initiates the visual signal, another functional process critical for photoreceptors is the visual cycle, which recycles and replenishes photopigment. Both processes are complex, consisting of multiple enzymatic and energetic steps. Disease-related disruption of the different steps may result in changes to different aspects or features of the ORG response. Therefore, it may be useful to devise methods for the quantitative description of these features. In particular, parameterization of ORG responses may result in multiple biomarkers that could potentially be linked to distinct aspects of photoreceptor function and homeostasis.

Here, we describe an optoretinographic imaging platform consisting of a full-field (FF), swept-source (SS), OCT system with adaptive optics (AO) and a visual stimulation channel. We used the system to measure ORG responses from two healthy subjects under a variety of stimulus conditions. We propose a four-parameter model that appears to describe the responses of cones to single-flash stimuli. We then discuss the extent to which the model can be used to analyze responses to more complex stimuli, such as multiple flashes and flashes delivered against adapting backgrounds. The

[1]Center for Human Ophthalmic Imaging Research (CHOIR), University of California, Davis Eye Center, Sacramento, CA 95817, USA. [2]Fisica de Materiais, Escola Politecnica de Pernambuco, Universidade de Pernambuco, 50720-001 Recife PE, Brazil. [3]Institute of Biomedicine, University of Turku, 20520 Turku, Finland. [4]EyePod small animal ocular imaging laboratory, Department of Cell Biology and Human Anatomy, University of California, Davis, CA 95616, USA.
*Corresponding author. Email: denise.valente@upe.br

model's capacity to quantify responses to single flashes and complex stimuli could support a unified theory of the ORG response, permit prediction of responses to diverse stimuli, and facilitate clinical translation of ORG methods.

RESULTS

Clear photoreceptor responses were observed in both subjects in each stimulus condition: single flashes, paired flashes, pulse trains, and adapting backgrounds. Responses to single flashes consisted of (i) a fast (~10 ms) early contraction stage; (ii) an elongation stage lasting hundreds of milliseconds; and (iii) a slow late contraction stage lasting several seconds, suggesting a return toward baseline length. The third stage was most obvious when recording for more than 1 s, especially when photopigment bleaching was low.

On the basis of qualitative analysis of the responses, the following model was proposed

$$\Delta\mathrm{OPL}(t) = u(t)\left[A_0 + A_1\left(-e^{-\tau_a \cdot t} + e^{-\tau_b \cdot t}\right)\right] \quad (1)$$

where $u(t)$ is the Heaviside step function. With the two exponential components, it was possible to represent the dynamics in stages 2 and 3. Stage 1, by contrast, is undersampled at the imaging rate of 400 Hz, which limited our ability to model that region of ORG response. By adding an offset A_0 to the function, it was possible to capture the amplitude of the shrinkage, an important figure of merit and potential biomarker. Without the A_0 component, the model is the solution to a differential equation describing overdamped oscillators (e.g., resistor-inductor-capacitor (RLC) circuits or springs).

Fits to this model and its variants (described in Materials and Methods) were qualitatively good and had low residual error (tables S1 and S2 in in Supplementary Materials). Results of the various stimulus conditions are described below.

Single flash

A representative measurement (subject 1, 8% cone bleach) is shown in Fig. 1A, along with the model fit. Optimal fit of the model was achieved with $A_0 = -36.4$ nm, $A_1 = 200.8$ nm, $\tau_a = 9.5\ \mathrm{s}^{-1}$, and $\tau_b = 0.07\ \mathrm{s}^{-1}$. Fits to all measurements were similarly qualitatively good, with $R^2 > 0.95$ and root mean square (RMS) error < 22 nm for all trials (see table S1). Figure 1B illustrates the good fit during the initial OS contraction and start of elongation. The four parameters of the model have distinct effects on the shape of the curve. These effects are illustrated in Fig. 1C for A_0 and Fig. 1D for A_1, τ_a, and τ_b.

In single-flash trials, measurements were performed in two subjects with various bleaching levels (Fig. 2) and fitted to the proposed model (Eq. 1). Measurements of the first subject were collected over 3 s after stimulus, while the second was measured for just 1 s. The reduced acquisition time in the second subject was motivated by the subsequent reductions in data transfer and processing times and data storage requirements. As shown below, this reduced time window appears primarily to impact estimation of the late contraction rate parameter (τ_b).

The effect of sampling duration on parameter estimation is illustrated in fig. S1 in Supplementary Materials, where the resulting percentage error for each parameter is depicted as a function of the observation window. An arbitrary level of 10% is plotted as a horizontal dotted line in each of the four plots. It can be observed that A_0 exhibits small variability, even with very short observation windows.

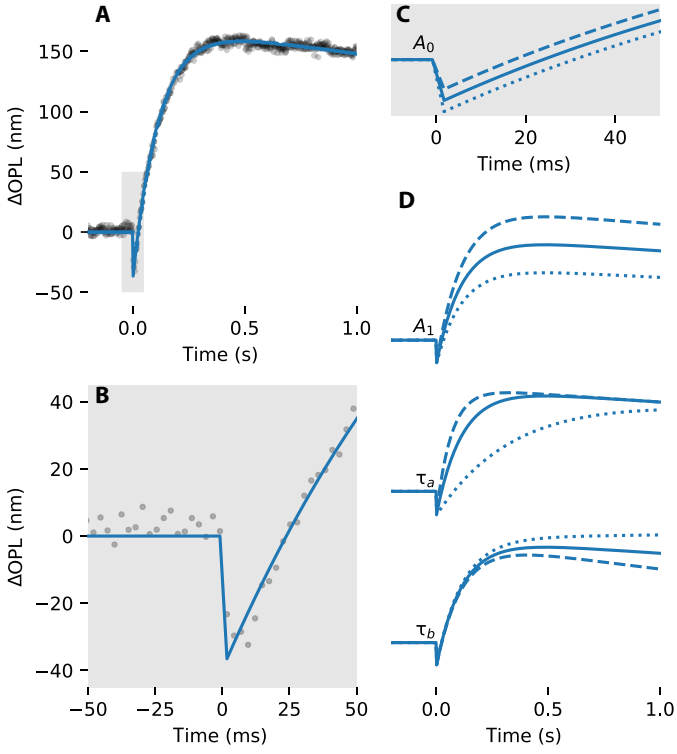

Fig. 1. Representative measurement and fit, and the effects of model parameters on response. (**A**) Representative measurement (subject 1, 8% cone bleach) plotted (gray circles), along with model fit (blue line). The gray box indicates the portion of the fitted response shown in (B). (**B**) Early portion of response and fit shown in detail. (**C**) Illustration of the effect of parameter A_0 on the ORG response, mainly seen in the amplitude of the initial OS contraction. (**D**) Illustrations of the effects of parameters A_1, τ_a, and τ_b on the ORG response. Dashed lines indicate more positive values, while dotted lines indicate less positive ones.

However, the other parameters demonstrate a need for longer observation times. It is apparent that A_1, τ_a, and τ_b require at least 1.05, 1.85, and 2.85 s, respectively, within this bleaching range, although A_1 and τ_a approach the 10% error level earlier for most bleaching levels. The most notable fluctuations are observed in τ_b, associated with the rate of the late contraction stage. The apparent convergence of error toward zero in the case of τ_b is an artifact of the analytical method because error is defined as a proportional difference from the 3-s estimate.

The fitted parameters resulting from both subjects' data using Eq. 1 are presented in Fig. 3. We observed a nonlinear, monotonic decay of A_0 with dose, leading us to fit the data to a sigmoidal Michaelis-Menten equation

$$A_0(b) = \frac{b \times v_m}{b + b_0} \quad (2)$$

with free parameters of $v_m = -54.6$ nm and $b_0 = 4.8\,\%$ and goodness of fit $R^2 = 0.85$ for subject 1 and $v_m = -30.5$ nm and $b_0 = 1.6\,\%$ and $R^2 = 0.97$ for subject 2. Although the limited number of data points (five per subject) raises concerns about overfitting, this choice is justified by key observations. Specifically, A_0 is expected to be zero at 0 % bleaching and to saturate as bleaching nears 100 %, a behavior well described by a rectangular hyperbola, like the Michaelis-Menten model, which naturally accounts for both the maximum

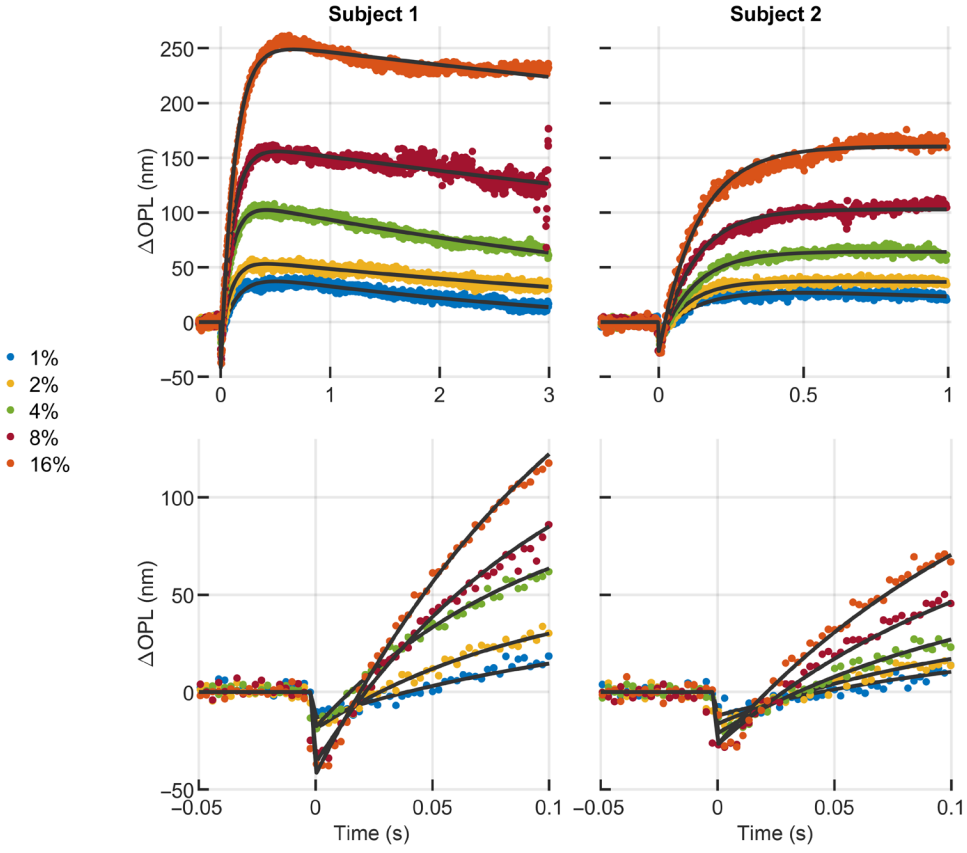

Fig. 2. Curve fitting of ORGs responses of two subjects in response to a single flash of 10 ms and different bleaching levels. (**Top**) The model provided visually good fits over a wide range of bleaching levels, whether ORGs were measured over 3 s (subject 1, left) or 1 s (subject 2, right). In both subjects, some aspects of the response were observed to vary monotonically with dose, such as the maximum excursion (ΔOPL_{max}) and slope of elongation between the flash and first ~100 ms increased with increasing bleaching fraction. Considerable variation between subjects was observed for given doses. This is most visible in the 16% trials, where the maximum OS excursion of subject 1 is at least 50% higher than that of subject 2. (**Bottom**) The model provided qualitatively good fits to the early contractile portion of the response as well, although similar intersubject variability is visible. The amplitude of the OS contraction and initial slope of elongation appear to scale with dose. The model has a discontinuity at $t = 0$ and, thus, does not capture features of the negative-going portion of the curve in the first 5 to 8 ms. This portion represents only two to three data points at the 400-Hz volume rate, which provide insufficient temporal resolution to model the initial contraction. Qualitative differences between the responses of the two subjects are exaggerated by the difference in duration of measurement: 3 s for subject 1 and 1 s for subject 2.

asymptote and the rate of approach toward it. Originally developed for enzyme kinetics, the Michaelis-Menten model has been widely applied across various biochemical processes (*26*). In ORGs, a similar dependence has been explored in the maximum excursion of rod photoreceptors (*20*). Although the mechanisms underlying early contraction amplitude and subsequent elongation differ, they likely share a comparable relationship with stimulus dosage.

The elongation amplitude term A_1 exhibited a nonlinear, monotonically increasing relationship to dose. Fitting A_1 to the Michaelis-Menten equation gives $v_m = 502.3$ nm and $b_0 = 11.1\%$ with $R^2 = 0.98$ for subject 1 and $v_m = 279.5$ nm and $b_0 = 8.4\%$ with $R^2 = 0.97$ for subject 2.

A curious result was obtained for elongation time constant τ_a, with a peak around 2% bleaching for both subjects. This may be an artifact of the relatively low signal-to-noise ratio of the 1% bleaching measurements and consequent underestimation of τ_a. The question merits further investigation, and, if the peak at 2% is reproducible, then it is an unexpected and interesting finding.

Last, τ_b was observed to decrease monotonically for both subjects. Due to the diminished confidence in this estimate using a 1-s measurement duration (see fig. S1), the analysis was restricted to subject 1. Those fitted parameters exhibited an apparent linear behavior on a semi-log scale, characterized by a slope of $-0.17\ s^{-1}$ and an intercept of $0.24\ s^{-1}$, with $R^2 = 0.84$. For completeness, the data for subject 2 were included in the plot, represented by unfilled markers.

Measurements were extended to higher bleaching levels (32 and 64%), as depicted in fig. S2. For these, the observation window was restricted to 1 s for both subjects because of the challenges in sustaining fixation after higher bleaching doses. Saturation in amplitude was not observed in either subject. The fitting diverges from the proposed model at these levels, which could indicate the presence of an additional exponentially rising, lower-amplitude component in response to higher energy stimuli, as discussed in (*27*). This hypothesis was investigated with a three exponential model (two rising and one falling), which revealed an improvement in the fit for high bleaching levels. The results for high bleaching levels are presented in the Supplementary Materials (fig. S2) and discussed in more detail in the "Comparison with other models" section. Alternative hypotheses include a divergence from linear behavior due to nonlinear

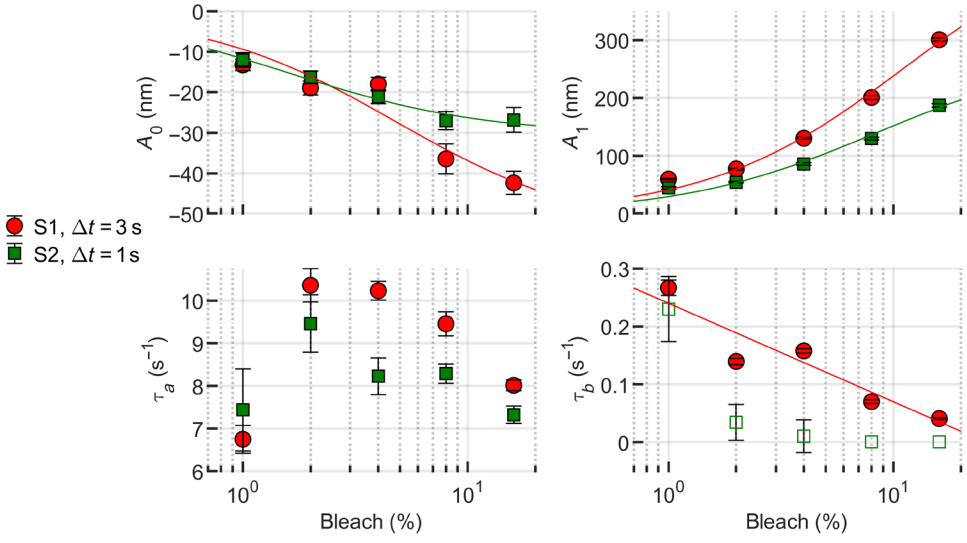

Fig. 3. Fitting parameters as a function of bleaching level. A_0, A_1, and τ_b exhibit well-behaved patterns, either monotonically growing or decreasing with dose. The qualitative observation that subject 1's responses, both the contraction portion and the elongation portion, were stronger than subject 2's is clearly visible in the plots of A_0 and A_1. Meanwhile, τ_a peaks at 2% bleaching for both subjects. A_0 and A_1 were fit with a sigmoidal Michaelis–Menten function, which fit both parameters in both subjects well ($R^2 \geq 0.85$). Based on the results shown in fig. S1, only the τ_b estimates from 3-s measurements from subject 1 were fit, this time with a log-linear model ($R^2 = 0.84$). Estimates of τ_b from subject 2's 1-s measurements are shown as unfilled markers. The error bars indicate the 95% confidence bounds of the fitting parameters. S1, subject 1; S2, subject 2.

biomechanical factors (e.g., drag or other hydrodynamic factors). However, the lack of data on the late contraction portion of ORGs at these bleaching levels limits our ability to model these factors.

Paired flashes

In both subjects, we measured responses to two successive flashes, each lasting 10 ms and having a power of 5.05 μW (equivalent to 4% single-flash bleaching). The flashes were separated by an interstimulus interval (ISI) denoted as t_{isi}, ranging from 15 to 300 ms.

Our observations revealed a cumulative, nonlinear effect when two equal flashes were presented. The cumulative response to two flashes that each bleach 4% of photopigment is equal in maximum excursion (~150 nm) to a single-flash bleaching 8% of photopigment, but smaller than twice the ~100 nm response to a 4% bleach. The response to two 4% flashes is shown in relation to single-flash responses in Fig. 4 (left). Flashes whose onsets were separated by as little as 15 ms result in distinguishable OS contractions, as seen in Fig. 4 (right).

The responses of cones to paired flashes had these characteristics over a range of ISIs between 15 and 300 ms, as seen in Fig. 5. Raw data are plotted with colored markers; fits to the shifted-sum, two-flash model described in Eq. 12 are plotted with a solid black line. Distinct contractile responses are visible for all first and second flashes [although the 15-ms ISI response is more visible in the zoomed view in Fig. 4 (right)]. Qualitatively, it can be seen that the magnitude of the second OS contraction appears to increase with increasing ISI. It also appears as though the elongation accompanying the second flash is attenuated when compared with the first. For example, in the $t_{isi} = 300$ ms response shown in Fig. 5 (right), the first flash appears to elongate the OS by ~100 nm and the second by ~50 nm.

Fitting with a sum of two time-shifted single-flash (Eq. 1) functions yielded estimates of eight free parameters, four for each of the two responses, labeled α and β for clarity: contraction amplitudes $A_{0,\alpha}$ and $A_{0,\beta}$; elongation amplitudes $A_{1,\alpha}$ and $A_{1,\beta}$; elongation time constants $\tau_{a,\alpha}$ and $\tau_{a,\beta}$; and late contraction time constants $\tau_{b,\alpha}$ and $\tau_{b,\beta}$. The α parameters resulting from this model fit were very similar to those observed in the single 4% bleach trials from this subject. For each of these pairs, we sought to understand the relationship between the first and second response's parameters, i.e., the effect of the first flash on the second. To assess this, we visualized the ratios of the β to α estimates as functions of ISI t_{isi}. These ratios are shown in Fig. 6.

Trust in the fitting-based estimates of response parameters depended on the duration of measurement, as shown in fig. S1. Here, the ISI and total recording time both imposed limits on the number of samples used to estimate a parameter. Because the initial contraction is rapid, it can be estimated well with relatively few samples. The elongation amplitude A_1 and time constant τ_a require relatively more than 100 ms to estimate reliably; thus, we rely solely on the 200- and 300-ms ISI estimates. For intervals $t_{isi} \leq 100$ ms, we lack confidence in the accuracy of the A_1 and τ_a estimates. Because these measurements were all collected within 1 s, we are also tentative about estimates of τ_b for all t_{isi}. The tentative estimates of A_1, τ_a, and τ_b are plotted, for completeness, with unfilled markers.

The ratio $A_{0,\beta} / A_{0,\alpha}$ (Fig. 6, top left) bears a clear relationship to t_{isi}, with $A_{0,\beta}$ being attenuated in inverse proportion to t_{isi}. For the shortest ISI $t_{isi} = 15$ ms, the second contraction $A_{0,\beta}$ is less than half the magnitude of $A_{0,\alpha}$, despite the first flash having bleached only 4% of photopigment. The slope of a linear fit to the ratios was 2.30 and 2.26 for subjects 1 and 2, respectively, and, for both subjects, a ratio of 1 was reached when $t_{isi} \approx 0.3$ s.

For $t_{isi} \geq 200$ ms, fitting of A_1 and τ_a resulted in acceptably low fitting error. For both of these parameters, the ratio of second to first response was between 0.75 and 1, as shown in Fig. 6 (top right and bottom left, respectively). Unfortunately, because of the low reliability of the 15- and 100-ms fits, a trend is difficult to establish.

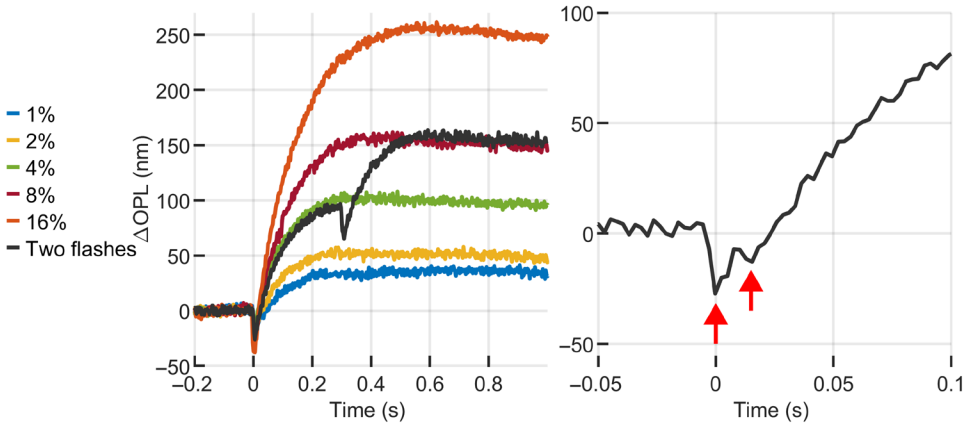

Fig. 4. Responses to paired flashes. (**Left**) The response to two sequential flashes of 4% bleaching exhibits a nonlinear cumulative effect, with maximum elongation equal to a single flash of 8% bleaching. (**Right**) Flashes as close as 15 ms apart can still be distinguished at the early response contraction.

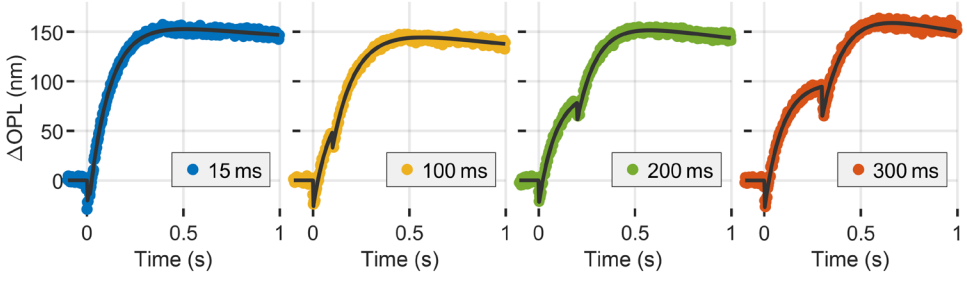

Fig. 5. Responses to pairs of flashes separated by ISI (t_{isi}) of 15, 100, 200, and 300 ms. Responses to two 4% flashes results in a total OS elongation of ~150 nm, equivalent to the elongation generated by a single 8% flash. However, the responses to multiple flashes are not simply the sums of individual responses. In the case of contraction, this can be seen in the magnitude of the early contraction, which seems to increase with increasing t_{isi}. In the case of elongation, the nonlinear additivity is most apparent in the case of t_{isi} = 300 ms, where the elongation caused by the second flash appears attenuated compared to that caused by the first. The maximum elongation for all four conditions was the same, and the overall amplitude of response of the second flash was reduced by the first.

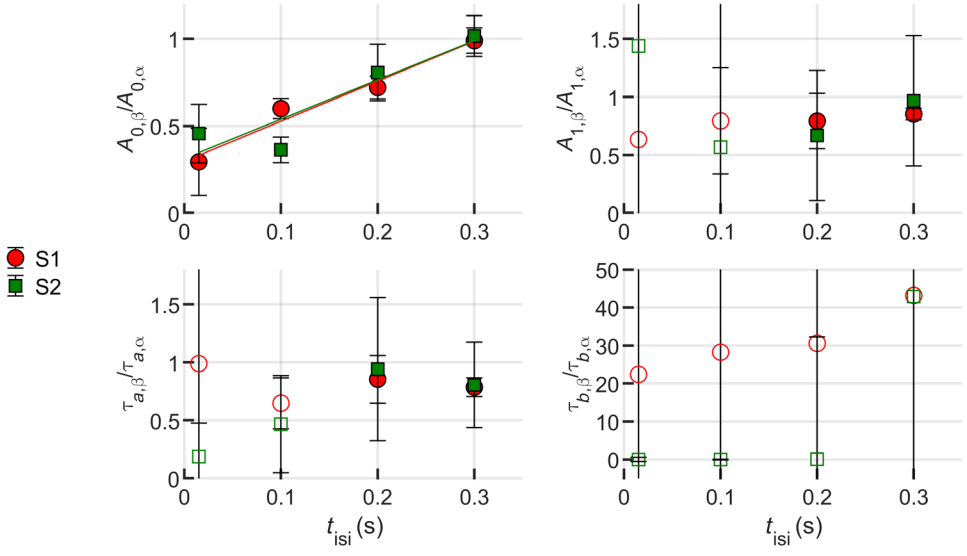

Fig. 6. Impact of the first flash on the second flash. The impact of the first flash on the second flash response was quantified by fitting the total response with the shifted-sum model shown in Eq. 12. From this fit, four free parameters could be estimated to describe the parts of the response due to each of the flashes, and the ratio of the second estimate to the first could be visualized as a function of ISI (t_{isi}). For A_0, a clear relationship with t_{isi} can be seen, with longer t_{isi} associated with higher A_0 magnitude. Differences between the A_1 ratio for t_{isi} = 200 ms and t_{isi} = 300 ms are visible but smaller than the error bars shown. For some parameters the observation window of the first flash was too small, leading to unreliable estimates. Those values are plotted with unfilled markers. All the values of τ_b falls into this category and are only shown here for completeness. Error bars were calculated by propagation of uncertainty of the confidence bounds of the fitting parameters. S1, subject 1; S2, subject 2.

To address uncertainty, error bars on the graph are computed by propagating the uncertainty arising from the confidence bounds obtained during the fitting process. Throughout the fitting procedure, the level of certainty of the free parameters was set as 95%, establishing lower and upper bounds. The width of this interval indicates the degree of uncertainty regarding the fitted coefficients. With that, the uncertainty of the ratio of given fitting parameters, for instance $A_{0,\alpha}$ and $A_{0,\beta}$, was determined using the variance formula for error propagation, assuming independence among the variables.

Stimulus pulse train

The attenuation of the ORG response due to the influence of a preceding flash, observed above, was corroborated through a sequence of multiple flashes. For this purpose, we recorded cone responses to a series of 1-ms flashes, each bleaching 4% of photopigment and separated by intervals of 50 ms. A distinct contraction was observed after the first few flashes, gradually diminishing in magnitude until it became indistinguishable from the background signal noise. This pattern of diminishing response aligns with the observations made during the paired flash stimulus experiments. The results of this experiment are shown in Fig. 7. No effort was made to fit these using the model because the t_{isi} of 50 ms does not permit reliable fitting of the responses. As discussed in the "Paired flashes" section and shown in fig. S1, a minimum gap of 200 ms between flashes is required to ensure robust fitting of A_0, A_1 and τ_a. While this limitation prevented further analysis in the current study, future measurements with longer pulse intervals and extended recording times could help explore this aspect further.

Adapting background

In these trials, following a 5-min period of dark adaptation, the studied region of the retina was exposed to a low-intensity background light for a duration of 10 s before data acquisition began. Subsequently, a single 10-ms flash with a photobleaching efficiency of 4% was administered.

The presence of the background light had a noticeable impact on the overall response dynamics (Fig. 8). It was observed that this background light caused sustained, apparently constant-rate OS elongation, to which the flash response apparently added. The response was thus modeled as the sum of a linear component and the single-flash response (Eq. 1)

$$\Delta\mathrm{OPL}(t) = u(t)\left[A_0 + A_1\left(-e^{-\tau_a \cdot t} + e^{-\tau_b \cdot t}\right)\right] + m \cdot t \qquad (3)$$

The resultant fitted parameters, as a function of background illumination, are shown in Fig. 9. It was observed that the slope (m) of the elongation due to the dim background line was directly proportional to the background light intensity, with proportionality constants given by 11.97 and 8.85 nm^3/photons for subjects 1 and 2, respectively.

These backgrounds bleached 0, 60, and 85% of photopigment in the 10 s before the stimulus flash. It is apparent that A_0, A_1, and τ_a are affected by the prior bleaching, as shown in Fig. 9. The magnitudes of A_0 and A_1 display a monotonic decay. The elongation rate τ_a shows an increasing trend with background intensity. The parameter τ_b falls within the minimum confidence window and is represented, for the sake of completeness, as unfilled markers.

The linear dependence observed under dim background light after exposure and a short recording period is likely valid only under similar conditions. With prolonged exposure and extended recording, the cone response may instead exhibit some form of saturation rather than a strictly linear trend.

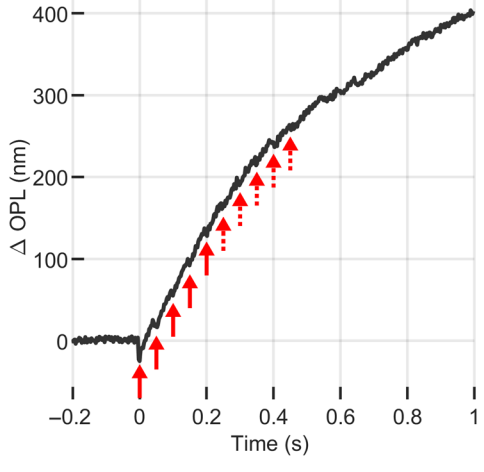

Fig. 7. Pulse trains. Optoretinography response to a series of 10 flashes of 10 ms, 4% bleaching flashes separated by 50 ms. It can be seen that the early stage contraction is increasingly attenuated by the presence of the previous flash (solid line arrows) until it gets hidden by the noise (dashed arrows).

DISCUSSION

We have reported stimulus-evoked cone photoreceptor responses measured with AO-FF-SS-OCT. AO-FF-SS-OCT joins a growing body of imaging modalities to have reported stimulus-evoked changes in OS length, including common-path interferometric methods (*14*, *16*), FF-SS-OCT with digital aberration correction (*15*), point-scanning AO-OCT (*17*, *18*, *20*), line-scanning AO-OCT (*28*), and conventional scanning OCT (*21*). This methodological diversity is a boon to the nascent field of ORG, as each presents unique advantages and will likely be the optimal choice for some problem domains. However, it presents a challenge as well because data produced by diverse methods are not inherently commensurate. Ultimately, we need to have quantitative methods for harmonizing measurements across these methods. Such harmonization is especially critical if ORG has commercial potential, as it may preempt analogous difficulties faced by researchers aggregating data from multiple OCT and OCT angiography instruments.

A critical step toward creating ORG standards is quantification of photoreceptor responses. Investigators in this area, thus far, have used ad hoc methods to do so, reporting the initial slope of elongation, maximum OS excursion, or principal components of concatenated responses (*17*, *20*, *21*). Such figures of merit have been useful but present potential disadvantages. Maximum (measured) OS excursion, for instance, is more vulnerable to noise than maximum OS excursion derived from a model fit. Initial slope of elongation is only accurate for a specific window of observation, whereas the time constant for an exponential elongation term is accurate over arbitrary windows of observation. The time to maximum OS length requires a minimum duration of measurement but could, in principle, be derived from a model fit even if the measurement duration is shorter than that time. Parameterization of signals always results in a loss of information, but multiple parameter fits lose less than single ad hoc figures of merit. In particular, when the model

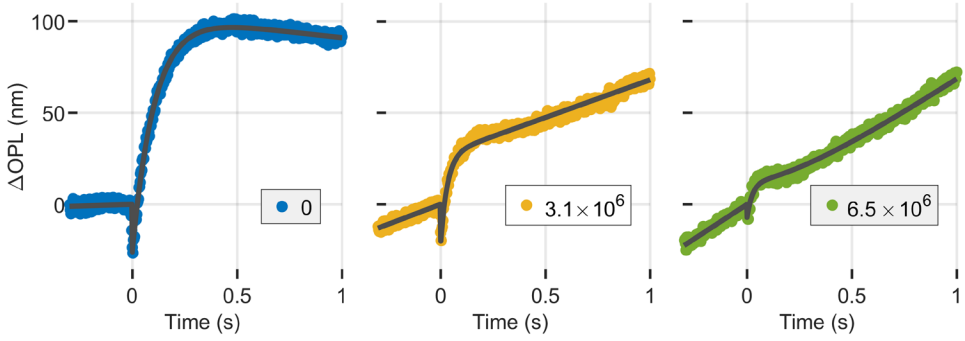

Fig. 8. Adapting background. Optoretinograms of a 4% flash in the presence of a dim background light using the same 555-nm source. Three powers, measured at the cornea, were used for the background: 0, 114, and 236 nW, which correspond to photon flux densities at the retina of 0, 3.1 × 10^6, and 6.5 × 10^6 s^{-1} μm^{-2}. After adapting for 10 s to the background light, the ORG presented a slope superposed to the response of the flash released at $t = 0$. The presence of background caused a reduction in both the contraction and elongation components of the cones' response to the flash.

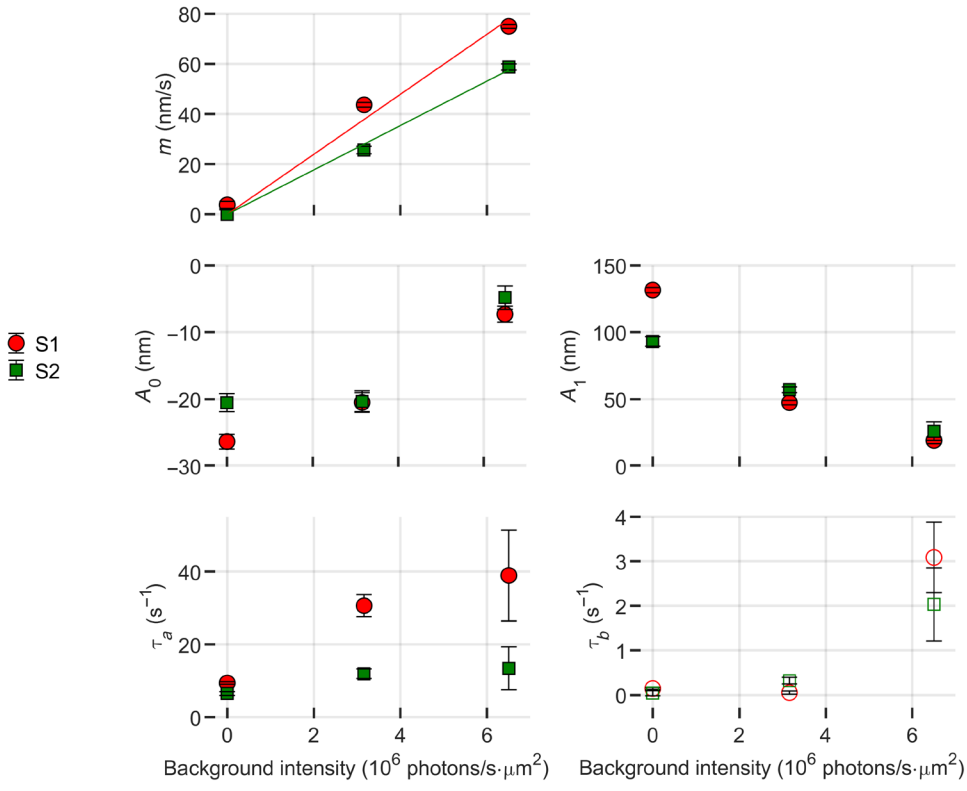

Fig. 9. Impact of a dim background on the flash response. Fitting parameters of Eq. 13 as a function of background illumination level. The constant elongation rate (m) appears to increase linearly with illuminance. The magnitudes of the contraction (A_0) and elongation (A_1) components of the response appear to be attenuated in the presence of a background. S1, subject 1; S2, subject 2.

can be used to derive those figures of merit, the former is preferred. Moreover, a general model of photoreceptor responses could be used, in conjunction with knowledge of the imaging system and signal processing techniques, to aggregate measurements from different imaging modalities.

A good ORG model will be sufficiently complex (measured in terms, e.g., of order and dimensionality) to represent distinct and possibly uncorrelated aspects of the response, but sufficiently simple to avoid overfitting and generation of meaningless dimensions. On the basis of our visual inspection of the ORG responses reported here and previously by our group, we felt that the model expressed by Eq. 1 strikes this balance. The model is intended to describe the dynamics of axial change observed in the cone OS. With only four parameters, the fitting equation allows direct access to key intuitive aspects of the ORG response: amplitudes of early contraction and elongation, and rates of elongation and late contraction. The purpose of this paper is to propose an initial working model, and we expect future work by us and others to refine it.

Single-flash responses

The early contractile response of the OS has been attributed to the early receptor potential, a change in charge distribution around opsin proteins following isomerization of their retinal chromophores by light (*19*). This electrical shift is hypothesized to cause repulsion among the membrane-bound opsins, which, in turn, flattens the discs and contracts the OS (*29*). The slower and larger magnitude elongation that follows has been shown to be suppressed in a transducin-knockout mouse model (*30*) and has been hypothetically attributed by several groups to swelling of the OS associated with increasing intracellular osmolarity. Quantitative characteristics of these responses, such as maximum and minimum excursion and initial elongation velocity, have been shown to depend on bleaching level by us and others (*15*, *17*–*21*).

Cone responses reported here were comparable to those reported by others. The 500-nm elongation observed at a bleaching level of 32% agrees roughly with previously reported 36% responses (*19*), and the 250-nm elongation observed at a bleaching level of 16% does as well (*18*). The absolute amplitude of the early contraction (A_0) was highest (~ -40 nm) at the highest bleaching level, consistent with the saturation of this component observed in both studies (*18*, *19*).

The model described by Eq. 1 appears qualitatively to capture the main features of the ORG response, as illustrated by Figs. 1 and 2. As shown in table S1, the goodness of fit across all bleaching levels was high [coefficient of determination $\left(R^2\right) > 0.95$ for all measurements, and $R^2 > 0.99$ for most], which confirms the visual goodness of fit shown in Figs. 1 and 2. The goodness of fit was high even in the case of high (≥32%) bleaching levels, where the qualitative appearance of the fit (fig. S2) was not as good.

Figure 1 (C and D) illustrates the role of each of the model's free parameters on the pattern of OS deformation. Hypothetically, these components of the response may be tied to electrostatic effects of photoisomerization (*29*) (A_0), osmolar gradients (A_1), rates of osmosis (*27*, *30*) (τ_a), and phototransductive down-regulation or photopigment regeneration (τ_b). Dependence of these aspects of the response on experimental parameters such as stimulus characteristics, eccentricity, and OS length could form the basis of a normative ORG database. Disease-related deviations from the resulting norms could potentially then be expressed in terms of the model parameters, which, in conjunction with the clinical workup, could lead to specific, testable hypotheses about disease mechanisms. Conversely, when disease etiology is known, such deviations could supply natural experiments to further elucidate the mechanisms of the ORG.

Standardization with alternative ORG metrics and implementations

As described above, interoperability of ORG methods is a key motivation for this work. As such, to compare with previous works, we derived a few figures of merit from the main model. Ad hoc figures of merit that have been reported include the early elongation slope m_0, time to maximum excursion $t_{\max}$, and maximum elongation $\Delta\mathrm{OPL}_{\max}$. These intuitive figures of merit can be derived from the derivative of $\Delta\mathrm{OPL}(t)$

$$\frac{d\Delta\mathrm{OPL}}{dt}(t) = u(t)\left[A_1\left(\tau_a e^{-\tau_a t} - \tau_b e^{-\tau_b t}\right)\right] + \delta(t)A_0 \tag{4}$$

While rate of early elongation is not well-defined, the elongation rate can be calculated at any desired time using Eq. 4. The root of Eq. 4 gives expressions for $t_{\max}$ (Eq. 5) and $\Delta\mathrm{OPL}_{\max}$ (Eq. 6), the time at which maximum OS elongation is attained, and the ΔOPL at that time, respectively

$$t_{\max} = -\frac{\log\left(\frac{\tau_b}{\tau_a}\right)}{\tau_a - \tau_b} \tag{5}$$

$$\Delta\mathrm{OPL}_{\max} = A_0 - A_1\left[e^{\frac{\tau_a \log\left(\frac{\tau_b}{\tau_a}\right)}{\tau_a - \tau_b}} - e^{\frac{\tau_b \log\left(\frac{\tau_b}{\tau_a}\right)}{\tau_a - \tau_b}}\right] \tag{6}$$

The data collection was confined to only two volunteers, a decision driven by the substantial size of each generated file and the extensive time required for data processing. While this approach is useful for measuring the response of individual cones, it restricts the feasibility of large-scale data acquisition, crucial not only for establishing normative behavior of healthy retinae but also for offering clinical insight into pathologies. Another limitation is the high cost associated with sufficiently fast and high-resolution OCT systems, which restricts the number of groups able to develop such a system.

Alternative implementations include a method based on OCT phase velocity, where the velocity of retinal structures is monitored rather than their position (*21*). Planned future work includes reproduction of some of these results in a larger number of subjects using the velocity-based approach. That method allows measurement of cone responses without the need to track specific cells over time, thus dispensing with the needs for an AO subsystem, digital aberration correction, real-time tracking, and 3D segmentation and registration. Moreover, because the velocity and position of the OS reflectors are related by integration, there is potential to use the derivative of Eq. 1, shown in Eq. 4.

The observation of photoreceptor function can also be achieved through 2D imaging systems such as a fundus camera (*14*) and scanning light ophthalmoscope (SLO) (*16*). In these methods, there is no direct measurement of OS length, and functional responses are encoded in the individual cone photoreceptor reflectance. This change in brightness is hypothesized to be related to constructive and destructive interference from the light reflected at the photoreceptor inner segment–OS junction (ISOS) and cone OS tip (COST), thereby establishing a correspondence with OCT measurements (*31*). While the 2D approach does not directly capture morphological changes, it offers the advantages of more affordable setups and substantially smaller volumes of data per ORG acquisition. The model proposed in this work could be used to model cone responses measured in en face, common-path interferometry, using an equation such as

$$\Delta I(t) = C_1 + C_2\cos\left[\frac{n\cdot 4\pi}{\lambda}A_1\left(-e^{-\tau_a\cdot t} + e^{-\tau_b\cdot t}\right) + \phi_0\right] \tag{7}$$

In principle, the parameters A_1, τ_a, and τ_b extracted from fits to coherent AO-SLO data could be compared directly with the same parameters extracted from fits to AO-OCT data using Eq. 1. Thus, the proposed model for light-evoked OS deformations could potentially serve as a valuable tool for directly comparing observed results across various OCT setups for ORG and potentially to act as a bridge

linking 2D measurements with the optical path length variation measured using OCT.

A brief review of ORG methods

As mentioned above, numerous investigators have measured stimulus-evoked changes in the outer retina. Some have observed changes in the amplitude of reflected or scattered light in animal models (*30*, *32*–*35*) and humans (*36*, *37*). Others have used the amplitude of the OCT signal to measure stimulus-evoked changes in outer retinal morphology (*38*–*40*). Notable among those outer retinal changes is a light-evoked change in OS length. The latter parameter has been studied more extensively by a number of groups, using various methods sensitive to the phase of the light reflected from the ends of the OS. One way to detect this length change is common path interferometry (*14*, *16*, *41*, *42*); however, this method has not yet been used successfully to quantify it. The main method that has been used to measure these submicron changes in OS length is phase-sensitive OCT, using either scanning or FF implementations (*15*, *17*–*21*, *27*, *28*, *43*, *44*). Broadly, the results presented here agree with these previously published findings. While these efforts have all measured OS length changes, the only one to have proposed a predictive model of such responses is Pandiyan *et al.* (*27*).

Comparison with other models

In addition to the model described by Eq. 1, a number of other models were considered. These models are listed in table S2 and visually depicted in Fig. 10. For clarity, we refer to them by the colors used in the plots in Fig. 10. Among these, three models were specifically developed to describe the early contraction phase:

1) Magenta: The triphasic model used in the above results, consisting of an instantaneous contraction, an elongation component, and a slow contraction component.

2) Orange: A variant of the triphasic magenta model, with a second, independent elongation component. Incorporation of this component was inspired by Pandiyan *et al.* (*27*).

3) Green: The magenta and orange models converge to A_0 as $t \to \infty$. To address this weakness, the triphasic green model was developed, which starts at the trough of the early contraction, captures the elongation and slow contraction phases, and converges to $\Delta OPL = 0$ as $t \to \infty$.

Figure 10 also includes three models that are not intended to describe the early contraction. For these, the responses were fitted by shifting the time axis so that $t = 0$ corresponds to the first zero-crossing of the response (~23 ms). We believe that this approach aligns with the method used by Pandiyan *et al.* (*27*), as suggested by their figure 2 (A to C). These models include the following:

4) Cyan: A monophasic model proposed by Pandiyan *et al.* (*27*), consisting of two rising exponential components with distinct amplitudes and time constants.

5) Blue: A biphasic simplification of the magenta model. It omits the initial contraction term and describes the elongation and late contraction.

6) Red: A monophasic simplification of the magenta model, reduced to a single exponentially rising term.

To compare models, each was used to fit an exemplary cone response to an 8% bleach. Residual errors ε were calculated only for $t > 0$, shifted accordingly. Within this short observation window of 1 s, all models fit the data reasonably well, as indicated by the low peak-to-peak fitting error ($|\varepsilon| \leq 10$ nm) shown in Fig. 10 (right). Fitting curves in Fig. 10 (left) were offset vertically by a few nanometers to improve visualization. The residual error, shown in Fig. 10 (right), suggests that the cyan and red models exhibit a low frequency component not present in the others. The RMS of the residual error was ~3 nm for the models that incorporated a late contraction component (magenta, orange, green, and blue) and ~4.5 nm for those that did not (cyan and red). The modestly higher fitting error and apparent low-frequency component in the latter may be due to a lack of the slow contraction term incorporated in the magenta, orange, green, and blue models. As anticipated, the difference in

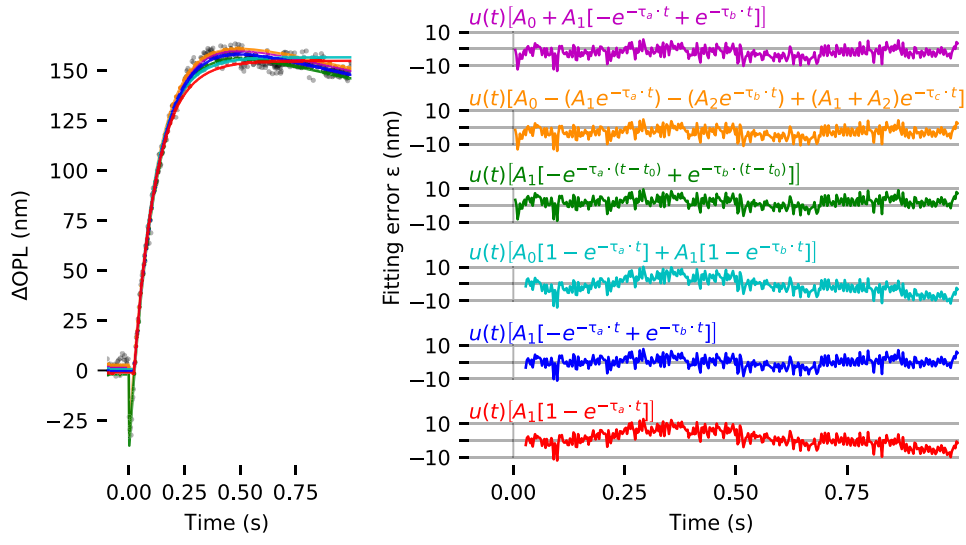

Fig. 10. Comparison among models and residual fitting error. (**Left**) Experimental data (subject 1, 8%) fitted with different models and **(right)** corresponding residual fitting error for each model. Residual error ε is only shown for the time span that the models are intended to describe: the full response for the magenta, orange, and green models and the response cropped at the first zero-crossing (~23 ms) for the cyan, blue, and red models.

residual error between models with and without a late contraction component becomes larger with longer observation windows, ~6 and ~11 nm, respectively, and the low frequency component becomes more apparent.

Performance of the magenta and green models was very similar. In Fig. 10, the two visually overlap and were offset by ±1 nm to facilitate visualization. Both models provide insights into early OS contraction, with the magenta model capturing amplitude and the green model focusing on its duration. We prioritized amplitude as a more intuitive descriptor.

In agreement with what was observed by Pandiyan *et al.* (*27*), the presence of two independent elongation components improved the fit for stronger stimuli ≥32%. This is apparent when comparing the triphasic (contraction/elongation/contraction) models: the one-elongation component magenta model to the two-elongation component orange model. This improvement is visible in fig. S2, and RMS fitting errors for all models are listed in table S2. For monophasic models designed only to describe the elongation of OSs, the two-component cyan model results in a better fit than the one-component red model.

For weaker stimuli, the goodness of fit achieved by the magenta model was comparable to that of the updated orange model, suggesting that the magenta model alone is sufficient to stimuli below 32% bleaching. Likewise, for weaker stimuli, the red model and cyan model performed similarly to one another.

Ultimately, the models with the lowest fitting error were the magenta model (for bleaching < 32%) and the orange model (for bleaching ≥ 32%). Moreover, these models quantify all three of the visible phases of the response—early contraction, elongation, and late contraction—each of which may confer independent scientific and clinical value. The cyan, blue, and red models may be of interest when imaging rates are too slow to measure the early contraction. An important implication of these findings is that the presence of a late contraction term in the model changes the optimal parameters for the elongation term(s). This is true, even when measurement is restricted to the first second after stimulation, when the elongation terms predominate. For example, the monophasic red curve and biphasic blue curve in Fig. 10 largely agree with one another visually and have similar residual fitting error, but the optimal estimates of their elongation amplitudes (A_1) and time constants (τ_a) differ by ~20%. This difference could be consequential if those estimates are used to generate hypotheses about underlying biochemical and biophysical mechanisms (*27*, *29*).

Complex stimuli

Other functions, derived from the model described in Eq. 1, were investigated to analyze more complex stimulus patterns, such as multiple flashes and a flash in the presence of a dim background. The main purpose of these experiments was to show that the proposed model can be used to quantify responses to complex stimuli. Of particular interest is the dependence of features of the ORG response, as quantified by model parameters, to previous light exposure, either single flashes, multiple flashes, or adapting backgrounds. Broadly, these dependencies are parameters of ORG light adaptation. Direct comparison of our findings with other measures of light adaptation is of uncertain value because their dependent variables—sensitivity thresholds in psychophysical detection, a-wave amplitudes in ERG, or photocurrents in single-cone suction pipette experiments—all depend on more complex mechanisms of inhibition and adaptation in the cone, retinal circuit, and brain.

Nevertheless, some observations may be of interest. First, in all three of these experiments, we observed that previous light exposure, one or more flashes or an adapting background, did affect ORG responses. In the case of paired flashes, the A_0 (early contraction) component was reduced, especially when the ISI was small, and the reduction in the A_1 (elongation) component was smaller (Fig. 6). At ISIs of 15 to 300 ms, paired flashes each bleaching 4% photopigment caused elongation equal to a single 8% flash, which is consistent with the reciprocity between stimulus duration and illuminance (or power) demonstrated using AO-SLO ORG (*42*). In the case of a train of 4% bleaching flashes, we failed to observe any A_0 component above response noise after approximately five flashes (a cumulative ~20% bleach). The early contraction component has previously been attributed to the early receptor potential (*19*, *29*), whose amplitude depends directly on numbers of photoisomerizations. Our observations that A_0 is attenuated by ~25% and ~50% due to bleaches of 4% and that the attenuation would depend on ISI at all may challenge that attribution. Alternatively, it may indicate that our model incompletely describes this component of the ORG response.

In the case of adapting backgrounds, notable reductions in the magnitudes of A_0 and A_1 were observed (Fig. 9). The total exposure of the cones to light before stimulus was much lower in the paired flash experiment (1.39×10^6 photons/μm^2) than in the adapting background experiment (3.1×10^7 and 6.5×10^7 photons/μm^2), which may be sufficient to explain the observed differences in ORG attenuation and may hint at a substantial role for photopigment availability. Although the attenuation of both A_0 and A_1 components was noteworthy, the fractional change was small compared to what has been measured using suction pipette measurements of single macaque cone photocurrents against adapting backgrounds (*45*), where reductions of several orders of magnitude were observed for comparable background levels. The difference may be because we did not achieve steady-state bleaching with the 10-s adaptation period, which we had hoped to do. Alternatively, it may suggest that the mechanisms of photocurrent adaptation differ from those of ORG adaptation. Notably, the attenuation of A_0 (early contraction) exhibited remarkable consistency across both subjects in the cases of paired flashes and adapting backgrounds. In future work, we plan to study the effect of adapting backgrounds more thoroughly.

Idiogenic variation among subjects and cells

One of the motivating goals of ORG research is the development of biomarkers for photoreceptor dysfunction. The sensitivity of these biomarkers will be limited by variation in response among healthy cells. Evident in the present work are both intersubject and intercone sources of such variability.

The differences in response between the two subjects are notable. Important demographic differences between the subjects include age difference, ethnicity, and associated pigmentation differences, sex, and eye length. While the lack of control for these variables is regrettable, our goal was to propose a general model of photoreceptor responses and not to quantify these sources of variability. Thus, the goodness of fit of our model, in spite of the obvious qualitative differences in response, suggests that the model is robust. Similar early ORG reports have also been limited in sample size and exhibit comparable intersubject variability (*27*). The sources of variability would be a practical topic of investigation if the number of independent variables (e.g., stimulus conditions) were smaller; future studies will pursue such a goal.

We also observed noteworthy variation in the response of cones. An example of this variation is shown in fig. S3 (top), where the ensemble mean response is plotted in opaque black, superimposed on every individual cone response, plotted in semitransparent black. The instantaneous SD of response was ~60 nm throughout the measurement. At the imaging location of 2° temporal to the fovea, we expect the fraction of S-cones to be low, between 4% (*19*) and 7% (*18*, *46*), and thus not a major contribution to the observed variability. The remaining L- and M-cones made up the vast majority of responding cells, and those were equally stimulated by the light-emitting diode (LED) wavelength of 555 nm, so we do not attribute the variability to spectral sensitivity differences among the cones. Potential causes for such variability include the length of the OS and its stage in the cycle of renewal and disc shedding; potential spatial variations in optical density of the inner retina, including capillaries; variation in extracellular biomechanical or hydrostatic factors; or temporal variation in response. Future studies will seek to quantify the variation among the responses of healthy cells, and possibly to identify sources of variability.

While the models were tested and characterized using only ensemble averages of cone response, the model can also be used to fit individual cone responses. An example of this is shown in fig. S3 (bottom). Future work may include fitting of individual responses to investigate the statistical dispersion of model parameters.

By allowing noninvasive, objective measurement of neural function in the retina, with the ability to localize functional responses and precisely observe structure-function correlations, the ORG offers complementary OCT-based biomarkers of functional responses of neurons and other structures. As such, it has the potential to transform clinical assessment of retinal disease and accelerate the development of novel therapeutics.

The presented model for light-evoked OS deformations offers a comprehensive understanding of the mechanical response observed in human cone photoreceptors following bleaching stimuli. This model, with only four parameters, allows direct access to crucial aspects of ORG responses, including the amplitudes of early contraction and elongation, as well as the rates of elongation and late contraction. The model fits well to the experimental data with a variety of stimulus intensity and patterns. Notably, the experimental data supporting this model were collected from only two subjects, underscoring the need for future studies with larger cohorts to establish a more generalized understanding of the average behavior in healthy retinas and its implications in pathological conditions.

MATERIALS AND METHODS

Imaging system

The imaging system has been reported in detail elsewhere (*47*). A schematic of the system is shown in fig. S4. Briefly, it consists of a Mach-Zehnder interferometer with a tunable light source (825 to 875 nm, BS-840-2-HP, Superlum, Cork, Ireland) divided into sample and reference arms by a polarizing beamsplitter. The reflected light goes to the sample arm and the transmitted light is expanded and collimated, striking the camera at an angle of ~1° with respect to the sample arm to create a spatially varying phase delay between the sample and reference fields and thus a carrier frequency. The resulting modulation of acquired interferograms allows the filtering in Fourier space of the retinal interference signal from DC components and common-path coherent artifacts (*48*), ensuring that the demodulated interferograms will consist only of signal generated by interference between the reference mirror and sample.

In the sample arm, light illuminated a 2° field of view on the retina with a converging (but not focused) beam with a power of 3 mW measured at the cornea. Ocular aberrations were corrected in real time by an AO subsystem operating in a closed loop using open-source software developed in Python/Cython by our lab (*49*). By measuring and correcting aberrations over a 6.75-mm-diameter pupil, it provided a diffraction-limited lateral resolution of 2.6 μm in the retina. A superluminescent diode (755 nm, 30-nm full width at half maximum) was used as AO beacon (IPSDM0701-C, Inphenix, Livermore CA, USA).

Sample and reference arms were recombined onto a high-speed 2D complementary metal-oxide semiconductor (CMOS) sensor (FASTCAM NOVA S-12, Photron, Tokyo, Japan) running at 200 kHz. The spectral sweep was sampled with 500 frames from the camera, which resulted in an OCT volume rate of 400 Hz. The camera's pixels are 20 μm wide, and magnification between the retina and camera was 22× (assuming a 16.7-mm focal length for the eye), and, thus, each pixel sampled ~0.9 μm in the lateral dimensions. The source swept over 50 nm of bandwidth between 875 and 825 nm, resulting in axial resolutions of 6.4 and 4.6 μm in the air and eye ($n = 1.38$), respectively. The retinal depth was sampled with an interval of 2.3 μm or frequency of 435 mm^{-1}.

Stimulus delivery and characterization

The setup incorporated a visible-light channel with control of flash time and power, designed for stimulating the retina. A fiber-coupled 565-nm light emitting diode (M565F3, with DC4100 four-channel LED driver; Thorlabs, Newton, NJ, USA) combined with a 23-nm band-pass filter centered at 555 nm (FF01-554/23; Semrock, Lake Forest, IL, USA) was used as light source. At this wavelength, L- and M-cones are bleached equally. The illuminated area was limited to a circle with diameter $\phi = 360$ μm due to the low power produced by the band-pass–filtered LED. A "top-hat" spatial distribution was used to ensure uniform illumination.

The stimulus pattern, delay, and duration were controlled using a function generator (Rigol DG4202, Suzhou, China), triggered by the CMOS camera. For a single flash, the resulting bleaching levels and corresponding optical powers and pulse duration are listed in table S3. Values correspond to an assumed ocular transmission of 1.0 and circular stimulated area with diameter 360 μm. Pulse width was 10 ms for all but the highest bleaching level of 64%, for which the pulse width was broadened to 12.6 ms. Bleaching percentages were calculated using methodology originally proposed by Rushton and Henry (*50*), and for which we previously published a detailed, step-by-step recipe (*21*).

Human subject imaging

Two subjects, free of known retinal disease, dark adapted, dilated, and cyclopleged using topical drops of phenylephrine (2.5%) and tropicamide (1.0%), were imaged at 2° temporal to the fovea. A bite bar and a forehead rest were used to position and stabilize the subject's pupil during imaging while a calibrated target guided the subject's fixation.

Subjects underwent a 5-min dark adaptation period before the imaging procedure. This involved placing the subject in a darkened room and covering the eye to be imaged with a patch. After the 5-min dark adaptation period and just before commencing the

imaging process, the subject was briefly exposed to ambient light within the darkened room for a few seconds to permit fixation and closing of the AO loop. OCT volumes were then acquired at a rate of 400 volumes per second for periods of 1 or 3 s, with the stimulus flash delivered after 200 ms.

All procedures were in accordance with the Declaration of Helsinki and approved by the University of California Davis Institutional Review Board. The simultaneous illumination from the three sources was in accordance with laser safety standards (*51*). Written informed consent was acquired from each subject, following an explanation of the experimental procedures and risks.

Stimulus patterns

Development of the ORG model described below was based on measurements using a single flash of the stimulus source. However, to demonstrate the feasibility of using more complex stimuli, additional patterns were used:

1) Single flash: Stimuli were delivered at varying bleaching levels. The flash duration was set at 10 ms for most trials, except for the 64% trial, for which the duration had to be extended to 12.6 ms to compensate the low power output provided by the bleaching light source.

2) Paired flashes: The subject received a pair of 4% flashes, separated by an ISI (t_{isi}) of 15, 100, 200, or 300 ms.

3) Pulse trains: A sequence of 4% flashes were administered with an interval of 50 ms between each flash. The first flash was initiated 200 ms after the commencement of data acquisition.

4) Adapting background: Single 4% flashes were delivered against an adapting background. The subject were given a 10-s period to adapt to the background before the flash was delivered. For adaptation, three powers, measured at the cornea, were used: 0, 114, and 236 nW, which correspond to photon flux densities of 0, 3.1×10^6, and 6.5×10^6 s^{-1} μm^{-2}. These backgrounds bleached 0, 60, and 85% of photopigment in the 10s before the stimulus flash.

All patterns were used for measurements on both subjects, with the exception of the "multiple-flash" pattern, which was measured in only one of the subjects.

Signal processing

The acquired spectral stacks were processed using a procedure described in detail elsewhere (*47*). In short, each acquired interferogram modulated by the off-axis carrier frequency was demodulated by 2D Fourier transform in *xy*, filtering in the Fourier space, shifting, and 2D inverse Fourier transformation. Next, a 1D short-time Fourier transformation in the spectral dimension was used to estimate fringe chirp due to system vibrations and/or group velocity dispersion mismatch. This chirp was then corrected by adding phase to the spectral stack accordingly. Last, the corrected spectral stacks were Fourier transformed into OCT volumes.

The acquired volumes underwent a flattening process to correct for the tilt caused by the off-axis approach. This flattening was performed by fitting a plane to the surface of the retina and shifting pixels accordingly. The volumes were then segmented axially, and the photoreceptor ISOS and COST layers were identified and aerially projected to produce en face images. These projections were registered to one another in the two lateral dimensions using cross-correlation to produce a trace of lateral retinal motion during image acquisition. The en face registered images are then averaged, and cones were automatically identified and individually segmented in three dimensions. The cone distribution exhibited a hexagonal packing, with a row-to-row spacing of ~4.5 μm at the imaged location of 2°. This corresponds to a center-to-center spacing of ~5.2 μm. Using the axial and lateral segmentation coordinates for each cone and the lateral eye movement trace, a volumetric region of interest ("subvolume") was extracted for each cone from each OCT volumetric image in the series. For each cone, ORG processing was performed on this series of cone subvolumes.

From each subvolume, a 3 by 3 grid of nine A-scans near the center of the cone were analyzed, occupying 2.7 μm by 2.7 μm. Each A-scan contained signal from the ISOS and COST surfaces. The phase difference between them at any given time [$\Delta\Phi(t)$] was calculated by computing the product of the complex COST pixel (A) and conjugate of the complex ISOS pixel (B) in each of the nine A-scans in the subvolume, computing the vector sum of these products, and lastly computing the angle of the vector sum

$$\Delta\Phi(t) = \angle \sum_{i=1}^{9} A_i \cdot B_i^* \tag{8}$$

The phase difference was then converted to optical path length difference by

$$\Delta\mathrm{OPL}(t) = \frac{\Delta\Phi\lambda}{4\pi} \tag{9}$$

where λ is the wavelength of the imaging beam.

A predictive model for light-evoked OS deformations

In trials in which the stimulus was a single flash, the resulting time series of phase differences exhibited a fast early contraction immediately after the flash onset, followed by a slower elongation, and an even slower late contraction. To provide a quantitative description of the early fast contraction, subsequent elongation, and late slow contraction, a four-parameter exponential model was used (Eq. 1)

$$\Delta\mathrm{OPL}(t) = u(t)\left[A_0 + A_1\left(-e^{-\tau_a \cdot t} + e^{-\tau_b \cdot t}\right)\right]$$

The four free parameters in this model are amplitudes A_0 and A_1 and time constants τ_a and τ_b. Time is represented by t, with flash onset at $t = 0$, and $\Delta\mathrm{OPL}(t)$ represents the change from baseline in OS optical path length at time t. $u(t)$ is the Heaviside step function, defined as

$$u(t) = \begin{cases} 0 & t < 0 \\ 1 & t \geq 0 \end{cases} \tag{10}$$

The data acquired for various stimulus levels were fitted to Eq. 1 in MATLAB (MathWorks, Natick, MA, USA) with a trust-region fitting algorithm (*52*). The parameters τ_a and τ_b were constrained to be nonzero positive values to prevent divergence of ΔOPL when $t \to \infty$. The fast contraction of the OS, because it occurs over only a few experimental data points, contributes a relatively small (1 to 3%) component the summed square error (SSE) during curve fitting. To ensure that this part of the response was accurately captured, data points in this region were weighted by a factor of 10, such that squared error in this region was multiplied by 10 before summation of SSE.

Optimization of ORG methods for clinical applications requires us to know how the duration of measurement affects estimation of model parameters. Longer measurements presumably provide more

repeatable parameter estimation, but at the expense of data processing and storage costs, especially because the data rate of the system is > 10 GB/s. To determine the effect of the duration of measurement on subsequent fitting, full 3-s measurements from subject 1 were fit with the model, and then truncated subsets of the data were fit with the same model. The effect of varying the data length on model parameters was expressed as a percentage error (PE) in fitting parameters (p) as a function of the data duration, with the full dataset (3-s observation window) used as the reference (p_r)

$$\mathrm{PE} = \frac{|p - p_r|}{p_r} \times 100 \tag{11}$$

For the proposed model to have predictive utility, i.e., to help predict the response of cones to arbitrary stimuli, the parameters of the model must be described as functions of stimulus dose. To achieve this, the relationships between model parameter estimates and dose were fitted as well using log-linear and Michaelis-Menten equations.

To quantify responses to two flashes (referred to as α and β) separated by an ISI of t_{isi}, responses were fit with a time-shifted sum of two single-flash models, described in Eq. 12. Quantifying responses to multiple flashes permits assessment of the additivity of single-flash responses

$$\begin{aligned}\Delta\mathrm{OPL}(t) &= \Delta\mathrm{OPL}_{\alpha}(t) + \Delta\mathrm{OPL}_{\beta}\left(t - t_{\mathrm{isi}}\right) \\ &= u(t)\left[A_{0,\alpha} + A_{1,\alpha}\left(-e^{-\tau_{a,\alpha}\cdot t} + e^{-\tau_{b,\alpha}\cdot t}\right)\right] + \\ &\quad u\left(t - t_{\mathrm{isi}}\right)\left\{A_{0,\beta} + A_{1,\beta}\left[-e^{-\tau_{a,\beta}\cdot\left(t - t_{\mathrm{isi}}\right)} + e^{-\tau_{b,\beta}\cdot\left(t - t_{\mathrm{isi}}\right)}\right]\right\}\end{aligned} \tag{12}$$

To quantify responses to flashes delivered after subjects had adapted to a dim background for 10 s, we modeled the response as a sum of the single-flash response (Eq. 1) and a linear ramp $m \cdot t$, where the slope of the ramp m is the rate of photopigment bleaching due to the background. The acquired data were fit to the following equation

$$\Delta\mathrm{OPL}(t) = u(t)\left[A_0 + A_1\left(-e^{-\tau_a\cdot t} + e^{-\tau_b\cdot t}\right)\right] + m \cdot t \tag{13}$$

Supplementary Materials

This PDF file includes:

Tables S1 to S3

Figs. S1 to S4

REFERENCES AND NOTES

1. W. L. Wong, X. Su, X. Li, C. M. G. Cheung, R. Klein, C. Y. Cheng, T. Y. Wong, Global prevalence of age-related macular degeneration and disease burden projection for 2020 and 2040: A systematic review and meta-analysis. *Lancet Glob. Health* **2**, e106–e116 (2014).
2. A. Anasagasti, C. Irigoyen, O. Barandika, A. López de Munain, J. Ruiz-Ederra, Current mutation discovery approaches in Retinitis Pigmentosa. *Vision Res.* **75**, 117–129 (2012).
3. C. X. Cai, J. G. Light, J. T. Handa, Quantifying the rate of ellipsoid zone loss in Stargardt disease. *Am. J. Ophthalmol.* **186**, 1–9 (2018).
4. T. Ben-Yosef, Inherited retinal diseases. *Int. J. Mol. Sci.* **23**, 13467 (2022).
5. K. Rohrschneider, S. Bültmann, C. Springer, Use of fundus perimetry (microperimetry) to quantify macular sensitivity. *Prog. Retin. Eye Res.* **27**, 536–548 (2008).
6. C. Kniestedt, R. L. Stamper, Visual acuity and its measurement. *Ophthalmol. Clin. North Am.* **16**, 155–170 (2003).
7. C. Owsley, Contrast sensitivity. *Ophthalmol. Clin. North Am.* **16**, 171–177 (2003).
8. A. G. Robson, L. J. Frishman, J. Grigg, R. Hamilton, B. G. Jeffrey, M. Kondo, S. Li, D. L. McCulloch, ISCEV Standard for full-field clinical electroretinography (2022 update). *Doc. Ophthalmol.* **144**, 165–177 (2022).
9. T. Y. Y. Lai, W. M. Chan, R. Y. K. Lai, J. W. S. Ngai, H. Li, D. S. C. Lam, The clinical applications of multifocal electroretinography: A systematic review. *Surv. Ophthalmol.* **52**, 61–96 (2007).
10. M. L. Gabriele, G. Wollstein, H. Ishikawa, J. Xu, J. Kim, L. Kagemann, L. S. Folio, J. S. Schuman, Three dimensional optical coherence tomography imaging: Advantages and advances. *Prog. Retin. Eye Res.* **29**, 556–579 (2010).
11. K. G. Csaky, E. A. Richman, F. L. Ferris, Report from the NEI/FDA ophthalmic clinical trial design and endpoints symposium. *Invest. Ophthalmol. Vis. Sci.* **49**, 479–489 (2008).
12. M. A. Choma, A. K. Ellerbee, C. Yang, T. L. Creazzo, J. A. Izatt, Spectral-domain phase microscopy. *Opt. Lett.* **30**, 1162–1164 (2005).
13. R. S. Jonnal, O. P. Kocaoglu, Q. Wang, S. Lee, D. T. Miller, Phase-sensitive imaging of the outer retina using optical coherence tomography and adaptive optics. *Biomed. Opt. Express* **3**, 104–124 (2012).
14. R. S. Jonnal, J. Rha, Y. Zhang, B. Cense, W. Gao, D. T. Miller, In vivo functional imaging of human cone photoreceptors. *Opt. Express* **15**, 16141–16160 (2007).
15. D. Hillmann, H. Spahr, C. Pfäffle, H. Sudkamp, G. Franke, G. Hüttmann, In vivo optical imaging of physiological responses to photostimulation in human photoreceptors. *Proc. Natl. Acad. Sci. U.S.A.* **113**, 13138–13143 (2016).
16. R. F. Cooper, W. S. Tuten, A. Dubra, D. H. Brainard, J. I. Morgan, Non-invasive assessment of human cone photoreceptor function. *Biomed. Opt. Express* **8**, 5098–5112 (2017).
17. M. Azimipour, J. V. Migacz, R. J. Zawadzki, J. S. Werner, R. S. Jonnal, Functional retinal imaging using adaptive optics swept-source OCT at 1.6 MHz. *Optica* **6**, 300–303 (2019).
18. F. Zhang, K. Kurokawa, A. Lassoued, J. A. Crowell, D. T. Miller, Cone photoreceptor classification in the living human eye from photostimulation-induced phase dynamics. *Proc. Natl. Acad. Sci. U.S.A.* **116**, 7951–7956 (2019).
19. V. P. Pandiyan, A. Maloney-Bertelli, J. A. Kuchenbecker, K. C. Boyle, T. Ling, Z. C. Chen, B. H. Park, A. Roorda, D. Palanker, R. Sabesan, The optoretinogram reveals the primary steps of phototransduction in the living human eye. *Sci. Adv.* **6**, eabc1124 (2020).
20. M. Azimipour, D. Valente, K. V. Vienola, J. S. Werner, R. J. Zawadzki, R. S. Jonnal, Optoretinogram: Optical measurement of human cone and rod photoreceptor responses to light. *Opt. Lett.* **45**, 4658–4661 (2020).
21. K. V. Vienola, D. Valente, R. J. Zawadzki, R. S. Jonnal, Velocity-based optoretinography for clinical applications. *Optica* **9**, 1100–1108 (2022).
22. X. Jiang, T. Liu, V. P. Pandiyan, E. Slezak, R. Sabesan, Coarse-scale optoretinography (CoORG) with extended field-of-view for normative characterization. *Biomed. Opt. Express* **13**, 5989–6002 (2022).
23. S. Chen, S. Ni, A. Jiménez-Villar, Y. Jian, Y. Jia, D. Huang, Optical coherence tomography split-spectrum amplitude-decorrelation optoretinography. *Opt. Lett.* **48**, 3921–3924 (2023).
24. A. Lassoued, F. Zhang, K. Kurokawa, Y. Liu, M. T. Bernucci, J. A. Crowell, D. T. Miller, Cone photoreceptor dysfunction in retinitis pigmentosa revealed by optoretinography. *Proc. Natl. Acad. Sci. U.S.A.* **118**, e2107444118 (2021).
25. B. J. Wendel, V. P. Pandiyan, T. Liu, X. Jiang, A. Lassoued, E. Slezak, S. Schleufer, P. Bharadwaj, W. S. Tuten, D. Mustafi, J. R. Chao, R. Sabesan, Multimodal high-resolution imaging in retinitis pigmentosa: A comparison between optoretinography, cone density, and visual sensitivity. *Invest. Ophthalmol. Vis. Sci.* **65**, 45 (2024).
26. B. Srinivasan, A guide to the Michaelis-Menten equation: Steady state and beyond. *FEBS J.* **289**, 6086–6098 (2022).
27. V. P. Pandiyan, P. T. Nguyen, E. N. Pugh Jr., R. Sabesan, Human cone elongation responses can be explained by photoactivated cone opsin and membrane swelling and osmotic response to phosphate produced by RGS9-catalyzed GTPase. *Proc. Natl. Acad. Sci. U. S. A.* **119**, e2202485119 (2022).
28. V. P. Pandiyan, X. Jiang, A. Maloney-Bertelli, J. A. Kuchenbecker, U. Sharma, R. Sabesan, R. Sabesan, High-speed adaptive optics line-scan OCT for cellular-resolution optoretinography. *Biomed. Opt. Express* **11**, 5274–5296 (2020).
29. K. C. Boyle, Z. C. Chen, T. Ling, V. P. Pandiyan, J. Kuchenbecker, R. Sabesan, D. Palanker, Mechanisms of light-induced deformations in photoreceptors. *Biophys. J.* **119**, 1481–1488 (2020).
30. P. Zhang, R. J. Zawadzki, M. Goswami, P. T. Nguyen, V. Yarov-Yarovoy, M. E. Burns, E. N. Pugh Jr., In vivo optophysiology reveals that G-protein activation triggers osmotic swelling and increased light scattering of rod photoreceptors. *Proc. Natl. Acad. Sci. U.S.A.* **114**, E2937–E2946 (2017).
31. M. Azimipour, D. Valente, K. V. Vienola, J. S. Werner, R. J. Zawadzki, R. S. Jonnal, "Investigating the functional response of human cones and rods with a combined adaptive optics SLO-OCT system," in *SPIE Proceedings 11218* (SPIE, 2020), pp. 43–52.
32. K. Bizheva, R. Pflug, B. Hermann, B. Považay, H. Sattmann, P. Qiu, E. Anger, H. Reitsamer, S. Popov, J. Taylor, A. Unterhuber, P. Ahnelt, W. Drexler, Optophysiology: depth-resolved probing of retinal physiology with functional ultrahigh-resolution optical coherence tomography. *Proc. Natl. Acad. Sci. U.S.A.* **103**, 5066–5071 (2006).
33. V. J. Srinivasan, T. H. Ko, M. Wojtkowski, M. Carvalho, A. Clermont, S. E. Bursell, Q. H. Song, J. Lem, J. S. Duker, J. S. Schuman, J. G. Fujimoto, Noninvasive volumetric imaging and morphometry of the rodent retina with high-speed, ultrahigh-resolution optical coherence tomography. *Invest. Ophthalmol. Vis. Sci.* **47**, 5522–5528 (2006).
34. P. Zhang, M. Goswami, R. J. Zawadzki, E. N. Pugh Jr., The photosensitivity of rhodopsin bleaching and light-induced increases of fundus reflectance in mice measured in vivo with scanning laser ophthalmoscopy. *Invest. Ophthalmol. Vis. Sci.* **57**, 3650–3664 (2016).

35. S. Gao, Y. Zeng, Y. Li, E. D. Cohen, B. A. Berkowitz, H. Qian, Fast and slow light-induced changes in murine outer retina optical coherence tomography: Complementary high spatial resolution functional biomarkers. *PNAS Nexus* **1**, pgac208 (2022).
36. P. DeLint, T. Berendschot, J. van de Kraats, D. van Norren, Slow optical changes in human photoreceptors induced by light. *Invest. Ophthalmol. Vis. Sci.* **41**, 282–289 (2000).
37. V. J. Srinivasan, Y. Chen, J. S. Duker, J. G. Fujimoto, In vivo functional imaging of intrinsic scattering changes in the human retina with high-speed ultrahigh resolution OCT. *Opt. Express* **16**, 12190–12200 (2008).
38. M. D. Abràmoff, R. F. Mullins, K. Lee, J. M. Hoffmann, M. Sonka, D. B. Critser, S. F. Stasheff, E. M. Stone, Human photoreceptor outer segments shorten during light adaptation. *Invest. Ophthalmol. Vis. Sci.* **54**, 3721–3728 (2013).
39. P. Zhang, B. Shibata, G. Peinado, R. J. Zawadzki, P. FitzGerald, E. N. Pugh Jr., Measurement of diurnal variation in rod outer segment length in vivo in mice with the OCT optoretinogram. *Invest. Ophthalmol. Vis. Sci.* **61**, 9 (2020).
40. A. Messner, V. Aranha dos Santos, H. Stegmann, S. Puchner, D. Schmidl, R. Leitgeb, L. Schmetterer, R. M. Werkmeister, Quantification of intrinsic optical signals in the outer human retina using optical coherence tomography. *Ann. N. Y. Acad. Sci.* **1510**, 145–157 (2022).
41. R. F. Cooper, D. H. Brainard, J. I. W. Morgan, Optoretinography of individual human cone photoreceptors. *Opt. Express* **28**, 39326–39339 (2020).
42. R. L. Warner, D. H. Brainard, J. I. W. Morgan, Repeatability and reciprocity of the cone optoretinogram. *Biomed. Opt. Express* **13**, 6561–6573 (2022).
43. S. Tomczewski, P. Węgrzyn, D. Borycki, E. Auksorius, M. Wojtkowski, A. Curatolo, Light-adapted flicker optoretinograms captured with a spatio-temporal optical coherence-tomography (STOC-T) system. *Biomed. Opt. Express* **13**, 2186–2201 (2022).
44. S. Tomczewski, P. Węgrzyn, M. Wojtkowski, A. Curatolo, Chirped flicker optoretinography for in vivo characterization of human photoreceptors' frequency response to light. *Opt. Lett.* **49**, 2461–2464 (2024).
45. L. H. Cao, D. G. Luo, K. W. Yau, Light responses of primate and other mammalian cones. *Proc. Natl. Acad. Sci. U.S.A.* **111**, 2752–2757 (2014).
46. C. A. Curcio, K. A. Allen, K. R. Sloan, C. L. Lerea, J. B. Hurley, I. B. Klock, A. H. Milam, Distribution and morphology of human cone photoreceptors stained with anti-blue opsin. *J. Comp. Neurol.* **312**, 610–624 (1991).
47. D. Valente, K. V. Vienola, R. J. Zawadzki, R. S. Jonnal, Kilohertz retinal FF-SS-OCT and flood imaging with hardware-based adaptive optics. *Biomed. Opt. Express* **11**, 5995–6011 (2020).
48. D. Hillmann, H. Spahr, H. Sudkamp, C. Hain, L. Hinkel, G. Franke, G. Hüttmann, Off-axis reference beam for full-field swept-source OCT and holoscopy. *Opt. Express* **25**, 27770–27784 (2017).
49. R. S. Jonnal rjonnal/ciao: Initial release -- stable and functional, Zenodo (2020); https://zenodo.org/record/3903941.
50. W. Rushton, G. Henry, Bleaching and regeneration of cone pigments in man. *Vision Res.* **8**, 617–631 (1968).
51. ANSI, *American National Standard for Safe Use of Lasers ANSI Z136* (Laser Institute of America, 2014).
52. T. F. Coleman, Y. Li, An interior trust region approach for nonlinear minimization subject to bounds. *SIAM J. Optim.* **6**, 418–445 (1996).

Acknowledgments: We acknowledge the assistance of clinical coordinator S. M. Garcia and helpful discussions with J. Werner, E. Pijewska, M. Bartuzel, R. Meleppat, and R. Maddipatla. **Funding:** This work was supported by National Institutes of Health [R01-EY-034340 (R.S.J./R.J.Z.), R01-EY-033532 (R.S.J.), R01-EY-031098 (R.J.Z.), R01-EY-026556 (R.J.Z.), and P30-EY-012576 (R.J.Z.)] and Research Council of Finland [356826 (K.V.V.)] **Author contributions:** R.S.J. conceived the research. D.V. and R.J.Z. designed the apparatus. D.V. constructed the apparatus. D.V. and R.S.J. developed the instrumentation software. R.J.Z., R.S.J., and D.V. designed the signal processing pipeline. D.V., R.S.J., and K.V.V. conducted the experiments. D.V. conducted the signal processing. All authors designed and conducted the data analysis. All authors wrote the manuscript. **Competing interests:** The authors declare that they have no competing interests. **Data and materials availability:** Data described here are available at https://zenodo.org/doi/10.5281/zenodo.11325119. All other data needed to evaluate the conclusions in the paper are present in the paper and/or the Supplementary Materials.

Submitted 30 May 2024
Accepted 7 May 2025
Published 11 June 2025
10.1126/sciadv.adq7332